

STFT-based Time-Frequency Mode Decomposition: A Fast and Robust Method for Multicomponent Signal Analysis

Wei Zhou^{a,b}, Wei-Jian Li^{a,b}, Wei-Xin Ren^{a,b,*}

^aCollege of Civil and Transportation Engineering, Shenzhen University, Shenzhen, 518061, China

^bNational Key Laboratory of Green and Long-Life Road Engineering in Extreme Environment (Shenzhen), Shenzhen University, 518060, China

Abstract

The decomposition of complex, multicomponent, and non-stationary signals into their constituent modes is a fundamental yet significant challenge in science and engineering. Existing methods often struggle with a trade-off among accuracy, computational cost, and the need for prior information such as the number of modes. This paper introduces time-frequency mode decomposition (TFMD), a novel framework for the fast, robust, and adaptive decomposition of such signals without requiring the number of modes to be specified a priori. TFMD operates on the principle that modes form contiguous high-energy regions in the time-frequency domain. Its non-iterative pipeline reframes signal decomposition as an image segmentation task: a signal is transformed into a spectrogram, which is then smoothed to enhance the continuity of these high-energy regions. A sequence of adaptive thresholding and connected-component labeling with size-based filtering is then employed to automatically segment the spectrogram and generate a mask for each mode. The modes are finally reconstructed via the inverse short-time Fourier transform. Validation on diverse synthetic signals demonstrates that TFMD accurately determines the number of modes and reconstructs them with high fidelity. Its performance is particularly strong in high-noise conditions. A comparative analysis confirms that TFMD provides robust, competitive performance across a wider variety of signal types, while a theoretical complexity analysis reveals its superior computational efficiency stemming from its non-iterative design. The method's practical utility is further demonstrated by successfully extracting modal responses from a real-world footbridge vibration signal. TFMD provides a computationally efficient and powerful paradigm for multicomponent signal analysis, offering a compelling balance of accuracy, versatility, and efficiency for large-scale or time-sensitive applications, with an implementation publicly available at <https://github.com/dopawei/TFMD>.

Keywords: Signal decomposition, Time-frequency analysis, Short-time Fourier transform, Connected-component labeling

*Corresponding author.

Email addresses: zhouw6@szu.edu.cn (Wei Zhou), weijianli@szu.edu.cn (Wei-Jian Li), renwx@szu.edu.cn (Wei-Xin Ren)

1. Introduction

The analysis of complex signals constitutes a cornerstone of advancement in numerous scientific and engineering disciplines, including but not limited to structural health monitoring (SHM) [1], biomedical engineering [2], acoustics [3], geophysics [4], and communications [5]. A significant proportion of real-world signals are inherently multicomponent, comprising several distinct constituent modes, frequently superimposed and exhibiting non-stationary characteristics such as time-varying frequency and amplitude. The extraction of meaningful information from such complex signals necessitates robust methodologies capable of decomposing them into their constituent modes. Such a decomposition must be effective even in the presence of noise, making algorithmic robustness a critical property. Effective signal decomposition is crucial for accurate system identification [6, 7], feature extraction [8], fault diagnosis [9, 10], and an improved understanding of the underlying physical phenomena.

Nevertheless, the decomposition of multicomponent, non-stationary signals into their constituent modes presents considerable challenges. Modes frequently overlap in both the time and frequency domains, rendering their decomposition difficult. The presence of noise can further obscure these modes, potentially leading to incorrect decomposition. While various signal processing techniques have been developed to address these issues, many existing methods encounter limitations. For instance, empirical mode decomposition (EMD) [11] and its variants [12, 13], while adaptive in nature, can suffer from mode mixing, end effects, and lack a strong mathematical framework. While variational mode decomposition (VMD) [14] provides a more structured decomposition, it typically requires the number of modes to be known beforehand. Additionally, its efficacy can be limited for certain non-stationary signals, as it models modes based on central frequencies, a characteristic that might not hold for those with rapidly changing instantaneous frequencies. To address this, variational nonlinear chirp mode decomposition extends the VMD framework by replacing these constant frequencies with time-varying instantaneous frequencies, though its performance is critically dependent on the quality of the initial estimates for these frequency paths [15]. Another significant category of approaches leverages Fourier spectrum-based decomposition, effectively employing bandpass-like filtering strategies defined in the frequency domain. This group includes methods such as the empirical wavelet transform [16] and empirical Fourier decomposition [17], which adaptively segment the Fourier spectrum to design filter banks; the Fourier decomposition method [18], which aims for a purely Fourier-based decomposition into intrinsic band functions; and Ramanujan Fourier mode decomposition [19], which utilizes Ramanujan sums for extracting periodicities. A fundamental and shared vulnerability of these techniques, stemming from their reliance on the global Fourier spectrum, is their limited ability to accurately separate non-stationary constituent modes that exhibit significant spectral overlap.

Furthermore, several techniques enhance time-frequency (TF) analysis or perform mode decomposition by post-processing the short-time Fourier transform (STFT) or wavelet transforms, or by utilizing STFT results to initialize more sophisticated models. The synchrosqueezing transform (SST) [20], for example, improves TF energy concentration by reallocating con-

tinuous wavelet transform coefficients based on instantaneous frequency (IF) estimates and allows for mode reconstruction. Building upon the principles of SST, the multisynchrosqueezing transform [21] employs iterative reassignment procedures to further concentrate TF energy and address issues such as non-reassigned points. The synchroextracting transform (SET) [22] and its variants [23, 24] refine the STFT by extracting only the coefficients that lie directly on the instantaneous frequency trajectory and discarding all others, thereby aiming to improve TF energy concentration with greater noise robustness than synchrosqueezing-based methods. Expanding on variational frameworks, where the STFT often serves to provide initial IF estimates, variational generalized nonlinear mode decomposition (VGNMD) [25] was developed to simultaneously extract chirp and dispersive modes by leveraging these STFT-derived TF ridges as initial guides for a variational optimization. Its enhancement, improved VGNMD [26], further refines this by introducing TF-skeleton extraction and weighted directional tracking to handle crossed modes, again often benefiting from STFT for initialization. Similarly, nonlinear chirp mode extraction [27] focuses on iteratively extracting a single desired nonlinear chirp mode using arctangent demodulation within a variational framework, where initial IF guidance can also be obtained from STFT. While these STFT-based and STFT-initialized techniques offer significant advancements over direct STFT or wavelet analysis by providing more resolved TF representations, they often introduce their own complexities, such as the selection of new parameters and/or computational burden. Consequently, despite the progress made by these various classes of methods, there remains a need for methods that can achieve accurate and robust decomposition with high computational efficiency and a reduced reliance on extensive, problem-dependent parameter tuning.

To address these prevailing challenges, the primary aim of this study is to introduce and validate a novel signal decomposition framework that achieves a superior balance of accuracy, robustness, and computational efficiency. The development of this framework is predicated on a central technical hypothesis: that constituent signal modes manifest as contiguous, high-energy regions in the TF domain, which are structurally distinguishable from the more diffuse or fragmented signature of noise. This work, therefore, seeks to demonstrate that a non-iterative pipeline based on TF masking can effectively exploit this structural difference to achieve highly adaptive and robust signal decomposition without requiring prior knowledge of the number of modes.

To achieve these aims, this paper puts forward time-frequency mode decomposition (TFMD). The methodology is realized through a direct, non-iterative pipeline that reframes signal decomposition as an image segmentation task: the signal’s STFT spectrogram is first smoothed to enhance the continuity of high-energy regions. An adaptive threshold is then applied to create an initial binary mask, on which connected-component labeling (CCL) is performed to identify distinct regions of 1-valued pixels. These regions yield a set of candidate masks, which are subsequently filtered by size to automatically determine the number of modes and produce a final set of filtered masks. Each filtered mask is then used to isolate the corresponding STFT coefficients for reconstruction into a time-domain mode via the inverse STFT (ISTFT). The

primary contributions and innovative aspects of TFMD are fourfold:

1. **Computational Efficiency:** It introduces a non-iterative framework with a quasi-linear theoretical time complexity, making it inherently more efficient than conventional iterative or quadratic-complexity methods and suitable for large-scale or real-time data analysis.
2. **Data-Driven Adaptivity:** It automatically determines the number of modes by filtering candidate masks based on their size, eliminating the need for this critical parameter to be specified a priori—a common limitation of methods like VMD.
3. **Inherent Robustness:** It integrates spectrogram smoothing and size-based mask filtering directly into the pipeline, providing intrinsic robustness to noise by design, particularly in high-noise scenarios.
4. **Versatility and Balance:** The methodology is conceptually straightforward and demonstrates a compelling balance of accuracy and general robustness across a diverse range of non-stationary signals.

This paper is organized as follows. Section 2 provides a detailed technical description of the TFMD methodology. Section 3 outlines the comprehensive validation framework, including the synthetic and real-world datasets, performance metrics, and benchmark algorithms. Section 4 presents the quantitative and qualitative results from all experiments. Section 5 provides a theoretical analysis of the computational complexity of the proposed method and its counterparts. Section 6 interprets these findings, discussing the implications, advantages, and limitations of the proposed method. Finally, Section 7 summarizes the key contributions and suggests directions for future research.

2. Time-Frequency Mode Decomposition

This section provides a detailed technical description of the proposed TFMD methodology. Following the conceptual framework of treating signal decomposition as an image segmentation problem, the entire non-iterative pipeline is presented in Figure 1, which serves as a visual guide for the key stages discussed in the following subsections.

2.1. Short-Time Fourier Transform and Spectrogram Generation

2.1.1. Short-Time Fourier Transform with Centered Frequencies

The first step is to obtain a TF representation of a discrete-time signal $x[n]$ using the STFT. The STFT coefficients $S[k, m]$ for frequency bin k and time frame m are defined as [28]:

$$S[k, m] = \sum_{n=-\infty}^{\infty} x[n]w[n - (m - 1)R]e^{-j2\pi F(k)n/f_s} \quad (1)$$

where $w[n]$ is the analysis window of length L_w , R is the hop size, and f_s is the sampling frequency. This produces a complex-valued STFT coefficient matrix $S \in \mathbb{C}^{N \times M}$ over the full TF domain $\Omega_{\text{Full}} = \{(k, m) \mid 1 \leq k \leq N, 1 \leq m \leq M\}$.

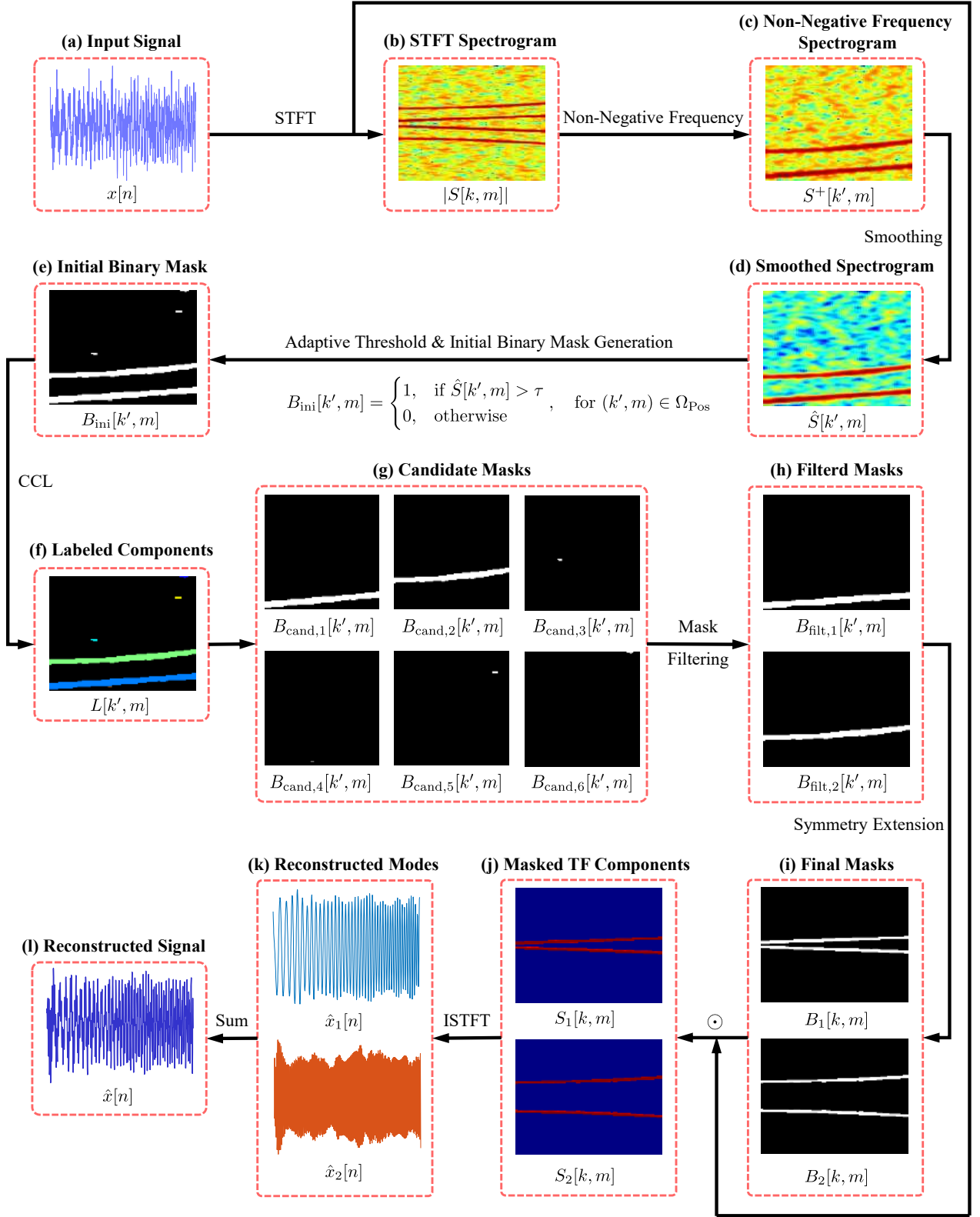


Figure 1: Flowchart of the proposed TFMD methodology. The process starts with (a) the input signal $x[n]$, which is transformed by the STFT to yield (b) the complex coefficients $S[k, m]$ and their corresponding spectrogram $|S[k, m]|$. The (c) non-negative frequency portion of the spectrogram is then (d) smoothed to produce a smoothed spectrogram $\hat{S}[k', m]$, which highlights high-energy TF regions. (e) An initial binary mask $B_{\text{ini}}[k', m]$ is generated via adaptive thresholding. (f) CCL is applied to identify distinct regions of connected 1-valued pixels, assigning a unique label to each region in the labeled components $L[k', m]$. (g) These regions are isolated as candidate masks $B_{\text{cand},i}[k', m]$. These masks are then (h) filtered by size to remove masks that may be generated by noise artifacts, yielding a set of filtered masks $B_{\text{filt},i}[k', m]$. (i) The filtered masks are extended with frequency symmetry to create the final masks $B_i[k, m]$. These are used to (j) extract the masked TF component for each mode from the original STFT coefficients. (k) Finally, ISTFT reconstructs each masked TF component into a time-domain mode, and (l) these modes are summed to synthesize the final reconstructed signal $\hat{x}[n]$.

To simplify subsequent symmetry operations, we use a centered frequency configuration where the frequencies $F(k)$ span approximately $[-f_s/2, f_s/2)$. The DC component (zero frequency) is located at index $k_{\text{DC}} = \lceil \frac{N+1}{2} \rceil$. The frequency $F(k)$ for any bin k is given by:

$$F(k) = (k - k_{\text{DC}}) \frac{f_s}{N}, \quad \text{for } 1 \leq k \leq N \quad (2)$$

2.1.2. Extraction of Non-Negative Frequency Spectrogram

For real-valued signals $x[n]$, the STFT exhibits conjugate symmetry: $S[2k_{\text{DC}} - k, m] = S^*[k, m]$. This means all information is contained within the non-negative frequencies (DC and positive frequencies). To improve computational efficiency, we perform the main analysis on this portion of the spectrogram.

The non-negative frequencies correspond to indices $k \geq k_{\text{DC}}$. We extract these $N_{\text{pos}} = \lceil N/2 \rceil$ rows from the STFT coefficient matrix to form the non-negative-frequency STFT coefficients, denoted $S^+ \in \mathbb{C}^{N_{\text{pos}} \times M}$. The new frequency index k' (from 1 to N_{pos}) relates to the original index k by $k = k' + k_{\text{DC}} - 1$. The extraction is thus:

$$S^+[k', m] = S[k' + k_{\text{DC}} - 1, m], \quad \text{for } k' = 1, \dots, N_{\text{pos}} \quad (3)$$

The domain for this reduced representation is $\Omega_{\text{pos}} = \{(k', m) \mid 1 \leq k' \leq N_{\text{pos}}, 1 \leq m \leq M\}$. The corresponding spectrogram is $|S^+[k', m]|$.

2.2. Spectrogram Processing and Mask Generation

2.2.1. Spectrogram Smoothing

To enhance the continuity of high-energy TF regions and suppress random noise fluctuations, we apply a smoothing filter to the magnitude of the non-negative-frequency STFT, $|S^+[k', m]|$. The smoothed spectrogram, $\hat{S}[k', m]$, is computed by averaging values within a local rectangular neighborhood:

$$\hat{S}[k', m] = \frac{1}{|\mathcal{N}_{U \times V}|} \sum_{(u,v) \in \mathcal{N}_{U \times V}(k', m)} |S^+[u, v]| \quad (4)$$

where $\mathcal{N}_{U \times V}(k', m)$ is the set of indices in a $U \times V$ window centered at (k', m) . This spatial filtering helps merge fragmented parts of a single high-energy TF region and improves the robustness of the subsequent thresholding step.

2.2.2. Adaptive Threshold Calculation

To separate high-energy TF regions from background noise, we compute an adaptive global threshold τ . The threshold is designed to be sensitive to strong signal peaks while remaining robust to the overall noise floor. We achieve this by calculating the geometric mean of the maximum and median values of the smoothed spectrogram:

$$\tau = \sqrt{\frac{\max(\hat{S}) \cdot \text{median}(\hat{S})}{C_{\text{thresh}}}} \quad (5)$$

The use of the maximum value ensures sensitivity to the high-energy signatures of constituent modes, while the median provides a stable estimate of the background energy. The parameter C_{thresh} , which inversely adjusts the threshold level, was empirically set to 2 for all experiments. A larger C_{thresh} results in a lower, less stringent threshold.

2.2.3. Initial Binary Mask Generation

Utilizing the calculated threshold τ , an initial binary mask B_{ini} is created over the non-negative frequency domain Ω_{Pos} :

$$B_{\text{ini}}[k', m] = \begin{cases} 1, & \text{if } \hat{S}[k', m] > \tau \\ 0, & \text{otherwise} \end{cases} \quad (6)$$

This mask, B_{ini} , provides a binary map where 1-valued pixels correspond to high-energy TF regions. The connected regions within this mask will be further processed to distinguish constituent modes from noise artifacts.

2.3. Mask Identification and Filtering

This stage refines the initial mask by distinguishing regions corresponding to constituent modes from those corresponding to noise. It operates on the principle that a mode's TF signature results in a large, contiguous region in the binary mask, whereas noise produces smaller, fragmented regions.

2.3.1. Connected-Component Labeling

We apply 8-CCL to the initial mask B_{ini} to group connected 1-valued pixels into distinct regions [29]:

$$L[k', m] = \mathcal{C}_8\{B_{\text{ini}}[k', m]\} \quad (7)$$

The resulting labeled components L assigns a unique integer label $i \in \{1, \dots, N_c\}$ to each of the N_c detected regions. From L , we extract a candidate mask, $B_{\text{cand},i}$, for each candidate region i :

$$B_{\text{cand},i}[k', m] = \mathbb{I}_{L[k', m]=i}, \quad \text{for } i = 1, \dots, N_c \quad (8)$$

where \mathbb{I} is the indicator function. This process is illustrated in Figure 2, where each colored region in the labeled component corresponds to one such candidate mask.

2.3.2. Size-based Filtering of Candidate Masks

To distinguish masks corresponding to constituent modes from those corresponding to noise, we filter the candidate masks based on their size. The size P_i of each candidate mask is its total count of 1-valued pixels:

$$P_i = \sum_{(k', m) \in \Omega_{\text{Pos}}} B_{\text{cand},i}[k', m], \quad \text{for } i = 1, \dots, N_c \quad (9)$$

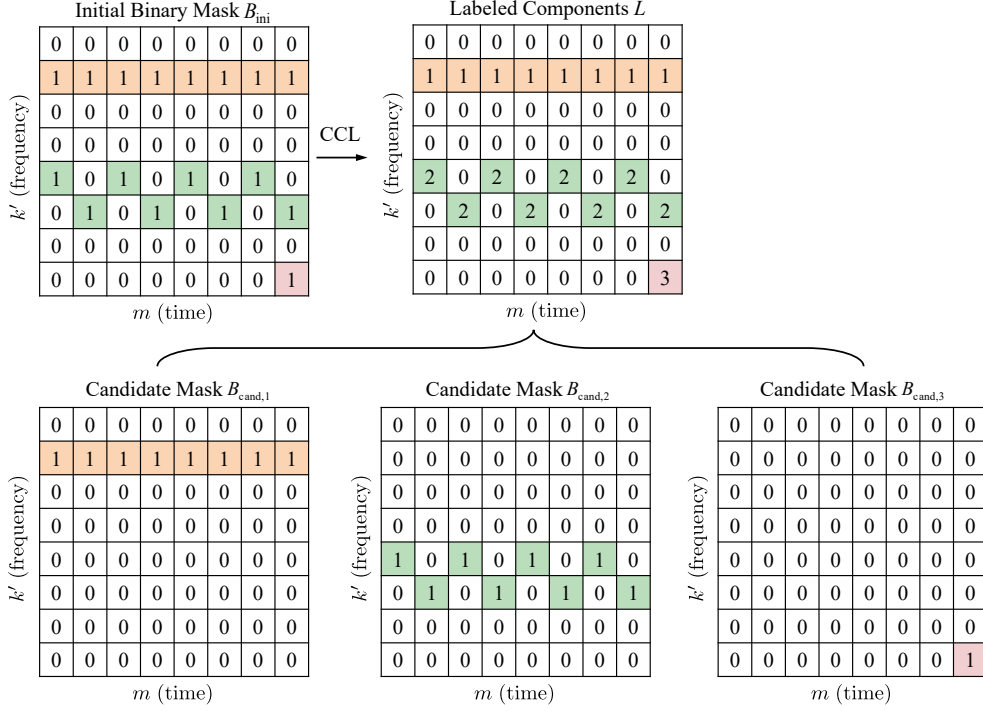


Figure 2: Illustration of the CCL process and candidate mask extraction. The top row shows the initial binary mask B_{ini} on the left, which undergoes 8-CCL to produce the labeled components L on the right, where each distinct connected region receives a unique label. The bottom row displays the candidate masks extracted from the labeled components. For instance, the third candidate mask, $B_{\text{cand},3}$, which corresponds to the isolated pink region, is a prime example of an artifact that would be discarded in the subsequent size-based filtering step due to its small area and lack of structural continuity.

A candidate mask is retained only if its size P_i exceeds a threshold. This threshold is defined as the larger of an absolute minimum size P_{abs} and a relative size, which is a fraction P_{rel} of the total number of pixels in the non-negative frequency spectrogram, denoted $|\Omega_{\text{Pos}}|$:

$$B_{\text{filt}} = \{B_{\text{cand},i} \mid P_i \geq \max(P_{\text{abs}}, \lfloor P_{\text{rel}} \cdot |\Omega_{\text{Pos}}| \rfloor)\}_{i=1}^{N_c} \quad (10)$$

The masks in this set, now re-indexed from $i = 1$ to $N_f = |B_{\text{filt}}|$, are denoted $B_{\text{filt},i}$ and termed the filtered masks. This size-based filtering step automatically determines the final number of modes, N_f .

2.3.3. Symmetric Mask Extension

Each of the N_f filtered masks, $B_{\text{filt},i}$, is now extended to the full TF domain Ω_{Full} to create a final mask, B_i . This is done by enforcing conjugate symmetry, which ensures that the subsequent reconstruction yields a real-valued time-domain mode. For each retained mask, we create its corresponding symmetric version by mirroring it around the DC frequency axis:

$$B_i[k, m] = \begin{cases} B_{\text{filt},i}[k - k_{\text{DC}} + 1, m], & \text{if } k \geq k_{\text{DC}} \\ B_{\text{filt},i}[k_{\text{DC}} - k + 1, m], & \text{if } k < k_{\text{DC}} \end{cases}, \quad \text{for } i = 1, \dots, N_f \quad (11)$$

2.3.4. Masked TF Component Extraction

Using the final masks, we now isolate the complex TF coefficients corresponding to each mode from the original, full STFT coefficient matrix S . The resulting masked TF component, S_i , is obtained by element-wise multiplication:

$$S_i[k, m] = S[k, m] \odot B_i[k, m], \quad \text{for } i = 1, \dots, N_f \quad (12)$$

This yields a set of masked TF components, $\{S_i\}_{i=1}^{N_f}$, each containing the complex TF coefficients corresponding to a single, isolated constituent mode.

2.4. Mode Reconstruction and Signal Synthesis

The final stage of TFMD is to transform the isolated masked TF components back into the time domain and reconstruct the final signal.

2.4.1. Inverse Short-Time Fourier Transform

Each isolated masked TF component S_i is transformed back into a time-domain mode $\hat{x}_i[n]$ using the ISTFT. The standard overlap-add method is used for reconstruction, which involves performing an inverse Fourier transform on each time frame and summing the overlapping, windowed results [28]. Conceptually, this operation is:

$$\hat{x}_i[n] = \text{ISTFT}\{S_i[k, m]\}, \quad \text{for } i = 1, \dots, N_f \quad (13)$$

The length of each reconstructed mode $\hat{x}_i[n]$ is adjusted to match the input signal length.

2.4.2. Final Signal Reconstruction

The final reconstructed signal, $\hat{x}[n]$, is obtained by summing all the N_f reconstructed modes:

$$\hat{x}[n] = \sum_{i=1}^{N_f} \hat{x}_i[n] \quad (14)$$

In summary, the TFMD methodology effectively decomposes the input signal into a set of meaningful time-domain modes, $\hat{x}_i[n]$, by identifying and isolating their corresponding high-energy, structurally coherent TF components. The final reconstructed signal $\hat{x}[n]$ thus represents the input signal with noise and spurious, disorganized artifacts significantly attenuated.

3. Experimental Design and Validation Setup

This section details the comprehensive experimental framework conceived to validate the TFMD methodology. The performance of TFMD is evaluated utilizing synthetic signals with known ground truth constituent modes and a real-world footbridge vibration signal. These experiments are designed to evaluate several key aspects of the algorithm's performance, including: its ability to automatically determine the correct number of constituent modes; the reconstruction fidelity of the individual modes and the overall signal; its robustness against noise; and its comparative performance against established techniques.

3.1. Datasets

3.1.1. Synthetic Signals

To facilitate a comprehensive performance assessment, a suite of six distinct synthetic signals, denoted $x_1(t)$ through $x_6(t)$, was designed. These signals encompass a range of complexities, including linear and nonlinear chirps, frequency modulation (FM) and amplitude modulation (AM), and transient events. Such characteristics are representative of the challenges encountered in analyzing real-world signals. Unless otherwise specified, all signals span a 1-second duration and were generated with a sampling frequency $f_s = 1000$ Hz. The ground truth constituent modes used to construct the composite signal $x_k(t)$ are denoted as $x_{k,j}(t)$. Multiple representations, including time-domain, frequency-domain, and TF representations, of these six synthetic signals are presented in Figure 3.

Signal Case 1: Frequency-Separated Chirps. This signal comprises two well-separated chirp-type constituent modes:

$$x_1(t) = \underbrace{1.0 \cdot \cos(2\pi \cdot [20t + 25t^2])}_{x_{1,1}(t): \text{Linear Chirp}} + \underbrace{0.9 \cdot \cos(2\pi \cdot [130t + 25t^3])}_{x_{1,2}(t): \text{Quadratic Chirp}} \quad (15)$$

The first constituent mode $x_{1,1}(t)$ is a linear chirp sweeping from 20 Hz to 70 Hz, while the second, $x_{1,2}(t)$, is a quadratic chirp sweeping from 130 Hz to 205 Hz. This case serves to evaluate the baseline decomposition capability of TFMD for clearly distinct, non-overlapping components.

Signal Case 2: Sinusoidal FM Signals. This signal consists of two sinusoidal FM constituent modes:

$$x_2(t) = \underbrace{1.2 \cdot \cos(2\pi \cdot 100t + 15 \sin(2\pi \cdot 2t))}_{x_{2,1}(t)} + \underbrace{1.0 \cdot \cos(2\pi \cdot 250t + 5 \sin(2\pi \cdot 5t))}_{x_{2,2}(t)} \quad (16)$$

Constituent mode $x_{2,1}(t)$ possesses an amplitude of 1.2, a carrier frequency $f_c = 100$ Hz, and is modulated at a frequency $f_m = 2$ Hz with a frequency deviation $\Delta f = 30$ Hz, resulting in a modulation index $\beta = \Delta f / f_m = 15$. Constituent mode $x_{2,2}(t)$ has an amplitude of 1.0, $f_c = 250$ Hz, $f_m = 5$ Hz, and $\Delta f = 25$ Hz, yielding $\beta = 5$. This case tests the algorithm's ability to track and separate multiple components exhibiting oscillatory frequency variations with different modulation parameters.

Signal Case 3: Four Components Mix. This complex signal combines four heterogeneous constituent modes:

$$\begin{aligned}
x_3(t) = & \underbrace{1.0 \cdot \cos(2\pi \cdot [10t + 15t^2])}_{x_{3,1}(t)} + \underbrace{0.9 \cdot \sin(2\pi \cdot 100t)}_{x_{3,2}(t)} \\
& + \underbrace{1.1 \cdot \mathbb{K}_{[0,0.7]}(t) \cdot \cos(2\pi \cdot 350(t - 0.1)) + 5 \sin(2\pi \cdot 6(t - 0.1))}_{x_{3,3}(t)} \\
& + \underbrace{1.2 \cdot \mathbb{K}_{[0.6,0.9]}(t) \cdot w(t) \cdot \sin(2\pi \cdot 200t)}_{x_{3,4}(t)}
\end{aligned} \tag{17}$$

Here, $\mathbb{K}_{[a,b]}(t)$ denotes the indicator function, equaling 1 for $t \in [a, b]$ and 0 otherwise. The function $w(t)$ represents a Tukey window with shape parameter $\alpha = 0.25$, applied over the interval $[0.6, 0.9]$. The constituent modes include a linear chirp sweeping from 10 Hz to 40 Hz, a pure tone at 100 Hz, a time-limited FM signal, and a transient AM burst. This configuration assesses the capability of TFMD to handle mixed signal types and intermittent temporal activity.

Signal Case 4: Low-Frequency Chirp and AM Tone. This case combines two constituent modes, one exhibiting FM and the other AM:

$$x_4(t) = \underbrace{1.0 \cdot \cos(2\pi \cdot [20t + 30t^2])}_{x_{4,1}(t)} + \underbrace{1.1 \cdot (0.8 + 0.4 \cos(2\pi \cdot 2t)) \cdot \sin(2\pi \cdot 200t)}_{x_{4,2}(t)} \tag{18}$$

Constituent mode $x_{4,1}(t)$ is a linear chirp sweeping from 20 Hz to 80 Hz. Constituent mode $x_{4,2}(t)$ is a 200 Hz tone whose amplitude is modulated at 2 Hz. This case tests the algorithm's effectiveness in signals with both FM and AM components.

Signal Case 5: Generalized Nonlinear Signal. This highly complex signal, with a duration of 3 seconds—that is, 3000 samples at $f_s = 1000$ Hz—incorporates seven challenging constituent modes. These include nonlinear chirps and signals synthesized from complex spectral definitions, designed to feature severely overlapping time-frequency signatures:

$$\begin{aligned}
x_5(t) = & \underbrace{\cos(2\pi \cdot (170t + 20t^2 + 3 \cos(3\pi t)))}_{x_{5,1}(t)} + \underbrace{\mathbb{K}_{[0,1.5]}(t) \cdot \cos(2\pi \cdot (75t + 20t^2))}_{x_{5,2}(t)} \\
& + \underbrace{\mathbb{K}_{[1,3]}(t) \cdot \cos(2\pi \cdot (10t + 20t^2 + 3 \cos(3\pi t)))}_{x_{5,3}(t)} + \sum_{j=4}^7 x_{5,j}(t)
\end{aligned} \tag{19}$$

where the signals $x_{5,j}(t)$ for $j = 4, \dots, 7$ are obtained via the inverse Fourier transform of their complex spectral definitions $\text{CDS}_j(f)$:

$$\text{CDS}_4(f) = 30e^{-j2\pi(0.4f+2\cos(2\pi f/100))} \cdot \mathbb{K}_{[f_s/4, f_s/2)}(f) \quad (20)$$

$$\text{CDS}_5(f) = 30e^{-j2\pi(0.8f+0.0005f^2)} \cdot \mathbb{K}_{[3f_s/10, f_s/2)}(f) \quad (21)$$

$$\text{CDS}_6(f) = 30e^{-j2\pi(1.8f+2\cos(2\pi f/100))} \cdot \mathbb{K}_{[7f_s/20, f_s/2)}(f) \quad (22)$$

$$\text{CDS}_7(f) = 30e^{-j2\pi(2.2f+0.0005f^2)} \cdot \mathbb{K}_{[4f_s/10, f_s/2)}(f) \quad (23)$$

The indicator functions in the frequency domain restrict these synthesized signals to specific frequency bands below the Nyquist frequency $f_s/2$. This case provides a stringent test for assessing the performance of TFMD when handling signals with severe nonlinearity, complex spectral phase structures, and significant time-frequency overlap.

Signal Case 6: Two Simple Tones. This fundamental case serves as a simple baseline with two stationary sinusoidal constituent modes:

$$x_6(t) = \underbrace{1.0 \cdot \sin(2\pi \cdot 100t)}_{x_{6,1}(t)} + \underbrace{0.8 \cdot \sin(2\pi \cdot 200t)}_{x_{6,2}(t)} \quad (24)$$

The constituent modes are pure tones at 100 Hz and 200 Hz. This case tests the fundamental frequency resolution capability of the proposed method.

3.1.2. Real-World Footbridge Vibration Signal

To evaluate TFMD's applicability to real-world engineering problems, this experiment utilized ambient vibration signal from the Dowling Hall Footbridge, a structure instrumented for SHM research [30, 31]. The primary objective was to apply TFMD to a representative vibration signal to decompose it into its constituent modes. The subsequent analysis aims to interpret these reconstructed modes in the context of structural dynamics, specifically to determine if they correspond to the physical modal responses of the structure.

Analyzing a single, short ambient vibration signal poses a significant challenge: due to the stochastic nature of the excitation, the TF representation of a constituent mode can appear fragmented and discontinuous, as illustrated in Figure 4(a). To address this, a prior-informed magnitude spectrogram was constructed to guide the mask generation process, as depicted in Figure 4(b). This prior was created by aggregating TF information from 157 distinct 5-minute signals recorded over several days (March 15-21, 2010). For each 5-minute signal from sensor Channel 1, the data were first decimated to 32 Hz and low-pass filtered at 12 Hz. The STFT was then computed (Gaussian window, $L_w = 128$, 90% overlap, $N = 256$), and the resulting magnitude spectrograms were individually normalized and summed. This composite prior, which exhibits more continuous and stable high-energy bands, was then used to generate masks for decomposing the single target 5-minute signal.

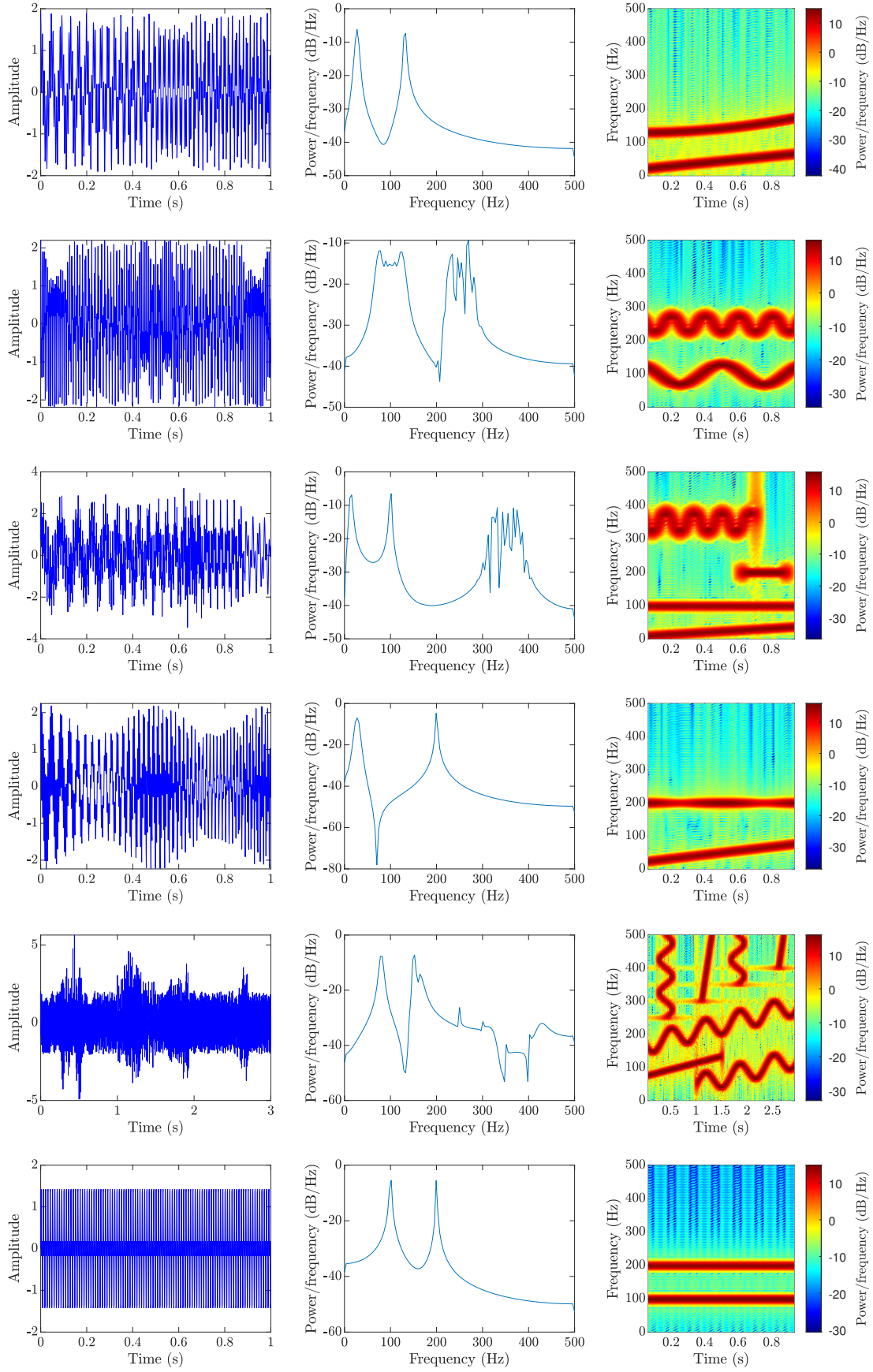


Figure 3: Time-domain (left), frequency-domain (middle), and TF representations (right) of the six synthetic signal cases. Spectrograms in the right column were generated utilizing the parameters detailed in Section 3.5. Rows correspond to Cases 1 through 6, respectively. Detailed signal descriptions are provided in Section 3.1.1.

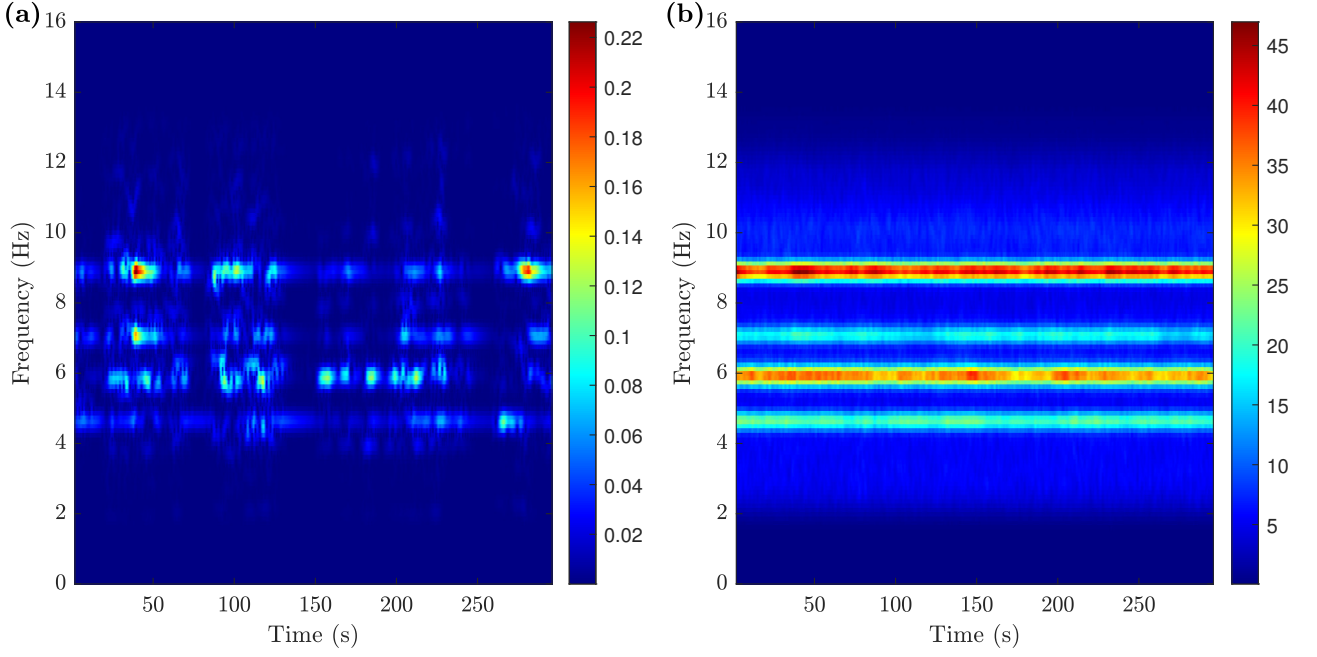


Figure 4: Comparison of STFT magnitude spectrograms for the Dowling Hall Footbridge data from Channel 1. (a) The STFT magnitude of the target 5-minute signal, showing fragmented energy regions. (b) The summed normalized STFT magnitude spectrogram constructed from multiple data segments, revealing more continuous and stable energy bands.

3.2. Performance Metrics

The quantitative assessment of decomposition and reconstruction performance relies on several key metrics. Let $y(t)$ represent a ground truth signal—either a constituent mode or the complete composite signal—and $\hat{y}(t)$ represent its corresponding estimate (reconstructed mode or reconstructed total signal) obtained from a decomposition algorithm.

First, the accuracy of the estimate $\hat{y}(t)$ relative to the ground truth $y(t)$ is evaluated using the relative L2 error, denoted \mathcal{E}_{rel} . This metric is defined as the ratio of the L2 norm of the estimation error to the L2 norm of the ground truth signal:

$$\mathcal{E}_{\text{rel}}(y, \hat{y}) = \frac{\|y(t) - \hat{y}(t)\|_2}{\|y(t)\|_2} \quad (25)$$

where $\|\cdot\|_2$ denotes the standard L2 norm, computed using its discrete equivalent for the sampled signals. Lower values of \mathcal{E}_{rel} indicate superior accuracy. This metric is utilized in two ways: first, to assess the fidelity of individual reconstructed modes $\hat{x}_{k,i}(t)$ after matching them to their corresponding ground truth constituent modes $x_{k,j}(t)$, yielding mode-specific errors denoted $\mathcal{E}_{\text{rel},j}$; and second, to evaluate the accuracy of the overall reconstructed signal $\hat{x}_k(t)$ compared to the input signal $x_k(t)$, yielding the total reconstruction error denoted $\mathcal{E}_{\text{rel, total}}$.

Second, to specifically quantify the performance in the presence of noise, as detailed in Section 4.2, the output SNR, denoted SNR_{out} , is utilized. This metric measures the quality of a reconstructed signal $\hat{x}(t)$ —obtained from potentially noisy input—relative to the noise-free

input signal $x(t)$. It is expressed in decibels (dB) as:

$$\text{SNR}_{\text{out}}(x, \hat{x}) = 10 \log_{10} \left(\frac{\|x(t)\|_2^2}{\|x(t) - \hat{x}(t)\|_2^2} \right) \quad \text{dB} \quad (26)$$

Higher SNR_{out} values signify better preservation of the input signal and more effective noise suppression during the reconstruction process.

3.3. Benchmark Algorithms

For comparative analysis, TFMD was benchmarked against several prominent and representative signal decomposition techniques from the literature: EMD [11], VMD [14], SET [22], adaptive chirp mode decomposition (ACMD) [32], and VGNMD [25].

3.4. Experimental Protocol

To comprehensively validate the proposed TFMD methodology, a series of experiments were designed and conducted as follows:

1. **Baseline Performance on Noise-Free Signals (Experiment 1):** The initial experiment focused on establishing the baseline performance of TFMD under ideal, noise-free conditions using the synthetic signals described in Section 3.1.1. The primary objective was to evaluate the algorithm's intrinsic ability to accurately separate known ground truth constituent modes and to reconstruct the input signal via its reconstructed modes.
2. **Noise Robustness Assessment (Experiment 2):** This experiment investigated the robustness and performance characteristics of TFMD when processing the synthetic signals contaminated by additive white Gaussian noise (AWGN) across various input SNRs, ranging from 5 dB to 40 dB.
3. **Comparative Analysis (Experiment 3):** This experiment aimed to benchmark the proposed TFMD methodology against the established signal decomposition techniques listed in Section 3.3, using noisy synthetic signals with input SNRs from 5 dB to 40 dB. This comparison assessed relative advantages and limitations in terms of SNR_{out} and reconstruction fidelity.
4. **Real-World Application (Experiment 4):** To evaluate TFMD on a real-world signal, this experiment utilized ambient vibration signals from the Dowling Hall Footbridge, with data processing detailed in Section 3.1.2. This experiment applied TFMD with a prior-informed spectrogram to decompose the signal and extract potential modal responses.

3.5. Implementation Details

All numerical simulations reported herein were executed using MATLAB R2024a. The computations were performed on a workstation equipped with a 13th Gen Intel(R) Core(TM) i7-13620H processor operating at a base frequency of 2.40 GHz and installed with 40.0 GB of RAM. For the proposed TFMD method, the parameters were configured as follows unless stated otherwise. A Gaussian analysis window was employed, defined by a length $L_w = 128$ samples.

The shape parameter α for the Gaussian window was set to 2.5 for most signal cases, but was adjusted to $\alpha = 2.0$ for Case 5 specifically to mitigate potential edge artifacts associated with its transient or abruptly starting/ending constituent modes. The analysis time frames overlapped by 115 samples, resulting in a hop size $R = L_w - 115 = 13$ samples and an overlap ratio of approximately 89.8%. The FFT size was set to $N = 256$. Spectrogram smoothing was performed using spatial averaging with a $U \times V = 3 \times 3$ kernel. The parameter C_{thresh} in the adaptive global thresholding method was set to 2. Subsequent TF component filtering based on pixel count utilized an absolute threshold $P_{\text{abs}} = 10$ pixels and a relative threshold $P_{\text{rel}} = 0.005$.

For the benchmark algorithms evaluated in Experiment 3, described in Section 4.3, parameters were selected following the recommendations in their respective original publications or common usage conventions. For instance, the number of modes for VMD was set equal to the known number of ground truth constituent modes for each test case.

4. Results

This section details the results obtained from the validation experiments outlined in Section 3. We first present the findings from Experiment 1, which evaluated the baseline performance of TFMD on noise-free synthetic signals.

4.1. Performance on Noise-Free Synthetic Signals

The primary objective of Experiment 1 was to evaluate TFMD’s inherent capability to separate known ground truth constituent modes and accurately decompose them as time-domain modes under noise-free conditions. The key quantitative results are summarized in Table 1 and Table 2.

Table 1: Overall reconstruction performance of TFMD on noise-free signals (Experiment 1). The table presents the number of ground-truth constituent modes (N_g), the number of modes identified by TFMD (N_f), the total relative L2 error for the reconstructed signal ($\mathcal{E}_{\text{rel, total}}$), and the average relative L2 error across the reconstructed modes ($\mathcal{E}_{\text{rel, avg}}$).

Case	N_g	N_f	$\mathcal{E}_{\text{rel, total}}$	$\mathcal{E}_{\text{rel, avg}}$
1	2	2	2.62×10^{-2}	5.14×10^{-2}
2	2	2	4.11×10^{-2}	4.34×10^{-2}
3	4	4	4.98×10^{-2}	5.11×10^{-2}
4	2	2	3.28×10^{-2}	5.98×10^{-2}
5	7	7	6.28×10^{-2}	5.76×10^{-2}
6	2	2	5.34×10^{-2}	4.44×10^{-2}

The performance of TFMD on noise-free signals demonstrates its effectiveness in both accurately identifying the number of modes and reconstructing the signal with high fidelity. As shown in Table 1, two key results stand out. First, the algorithm successfully determined the correct number of modes for all six signal cases; the number of identified modes, N_f , precisely matched the number of ground-truth constituent modes, N_g , in every instance, from simple

two-component signals to the complex seven-component case. Second, the overall reconstruction accuracy was consistently high. The total relative L2 error, $\mathcal{E}_{\text{rel, total}}$, remained low across all cases, ranging from a minimum of 2.62×10^{-2} for the well-separated chirps in Case 1, to a maximum of 6.28×10^{-2} for the challenging Case 5. These low error values indicate that the sum of the reconstructed modes provides a very close approximation to the input signal, thereby validating the signal synthesis process described in Equation (14).

Table 2: TFMD individual mode decomposition performance for Experiment 1 with noise-free signals. Values represent the relative L2 error \mathcal{E}_{rel} for the reconstructed mode $\hat{x}_{k,i}(t)$ that best matched the corresponding ground truth constituent mode $x_{k,j}(t)$. Columns correspond to the constituent mode index j .

Case	$\mathcal{E}_{\text{rel},j=1}$ ($\times 10^{-2}$)	$\mathcal{E}_{\text{rel},j=2}$ ($\times 10^{-2}$)	$\mathcal{E}_{\text{rel},j=3}$ ($\times 10^{-2}$)	$\mathcal{E}_{\text{rel},j=4}$ ($\times 10^{-2}$)	$\mathcal{E}_{\text{rel},j=5}$ ($\times 10^{-2}$)	$\mathcal{E}_{\text{rel},j=6}$ ($\times 10^{-2}$)	$\mathcal{E}_{\text{rel},j=7}$ ($\times 10^{-2}$)
1	5.29	5.00	—	—	—	—	—
2	3.70	4.97	—	—	—	—	—
3	5.54	4.96	8.05	1.90	—	—	—
4	4.78	7.18	—	—	—	—	—
5	6.96	4.09	8.74	4.14	4.57	5.33	6.49
6	3.53	5.35	—	—	—	—	—

Beyond the overall signal reconstruction, the fidelity of the individual reconstructed modes was also high. Table 2 details the relative L2 error for each reconstructed mode against its corresponding ground-truth constituent mode. The average mode error, $\mathcal{E}_{\text{rel, avg}}$, remained below 6.0×10^{-2} for all cases, as reported in Table 1. An examination of the individual mode errors reveals consistently strong performance. For instance, in Case 1, the two chirp modes were reconstructed with errors of only 5.29×10^{-2} and 5.00×10^{-2} . Even for the complex, four-component signal in Case 3, the errors for the reconstructed modes were low, ranging from 1.90×10^{-2} to 8.05×10^{-2} . While the highly complex signal in Case 5 presented the greatest challenge, most of its seven modes were still reconstructed with errors below 9.0×10^{-2} , with the highest individual error being 8.74×10^{-2} . These findings confirm that TFMD not only reconstructs the input signal accurately but also preserves the integrity of the individual constituent modes during the decomposition and reconstruction process.

Figure 5 provides a visual confirmation of the decomposition quality for Case 4. In Figure 5(a), the overall reconstructed signal $\hat{x}_4(t)$ is shown to be a close match to the input signal $x_4(t)$. In Figure 5(b) and (c), the reconstructed modes $\hat{x}_{4,1}(t)$ and $\hat{x}_{4,2}(t)$ are shown to accurately capture their ground truth constituent modes, $x_{4,1}(t)$ and $x_{4,2}(t)$, respectively. A key characteristic is evident across the error signals, which are plotted in each part of the figure and defined as the difference between the ground truth and the reconstructed signals (e.g., $x_4(t) - \hat{x}_4(t)$): while small in magnitude overall, they consistently exhibit larger amplitudes at the signal’s endpoints. Despite these boundary effects, the overall reconstruction quality remains high, as confirmed by the low total error ($\mathcal{E}_{\text{rel, total}} = 3.28 \times 10^{-2}$) and mode-specific errors (4.78×10^{-2} and 7.18×10^{-2}) reported in Table 2.

In summary, the results from Experiment 1 establish that the proposed TFMD method

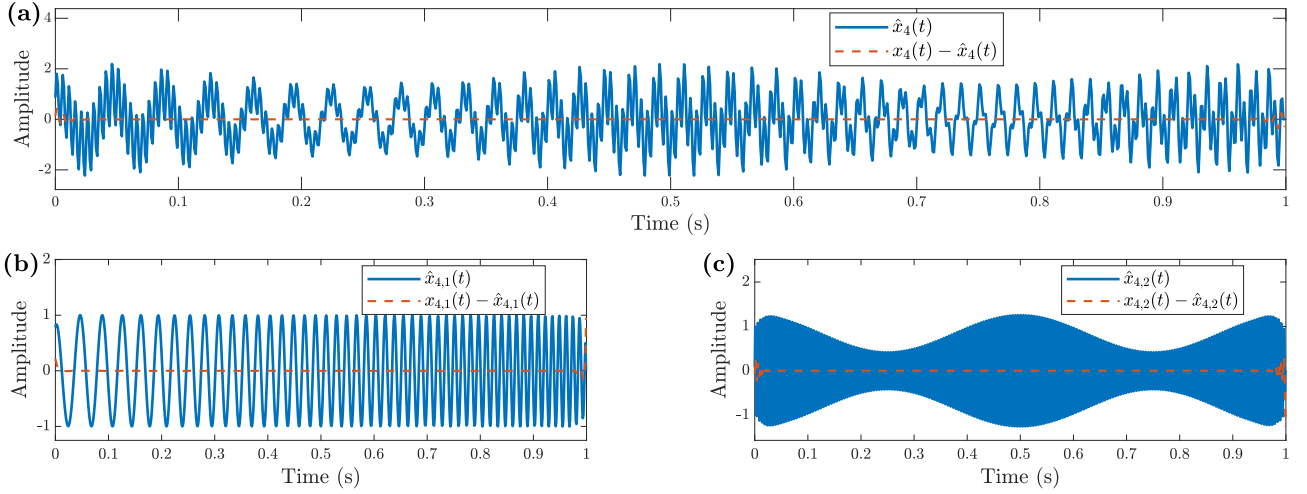


Figure 5: TFMD decomposition results for noise-free $x_4(t)$. (a) Comparison of the final reconstructed signal $\hat{x}_4(t) = \sum_i \hat{x}_{4,i}(t)$ (solid blue line) with the total reconstruction error $x_4(t) - \hat{x}_4(t)$ (dashed red line). (b) Comparison of the first reconstructed mode $\hat{x}_{4,1}(t)$ (solid blue line), corresponding to the ground truth constituent mode $x_{4,1}(t)$, with its estimation error $x_{4,1}(t) - \hat{x}_{4,1}(t)$ (dashed red line). (c) Comparison of the second reconstructed mode $\hat{x}_{4,2}(t)$ (solid blue line), corresponding to the ground truth constituent mode $x_{4,2}(t)$, with its estimation error $x_{4,2}(t) - \hat{x}_{4,2}(t)$ (dashed red line).

performs effectively on noise-free signals. The method demonstrates a strong capability to accurately determine the number of constituent modes and to reconstruct both the individual modes and the overall composite signal with high fidelity across a diverse set of test cases.

4.2. Noise Robustness Assessment

Experiment 2 evaluated the robustness of the TFMD algorithm against AWGN. The performance was assessed across a range of input SNRs, from a high-noise level of 5 dB to a low-noise level of 40 dB, for the six synthetic signal cases. The relationship between input signal quality and the resulting performance is illustrated in Figure 6 and detailed numerically for the representative Case 4 in Table 3.

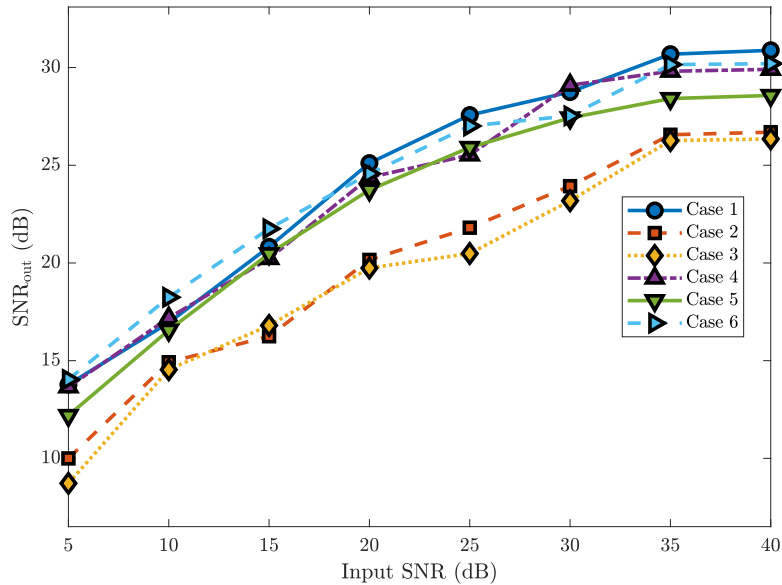


Figure 6: TFMD noise robustness assessment for all six signal cases. The plot shows the output SNR (SNR_{out}) as a function of the input SNR.

The results reveal a dual-faceted behavior of the TFMD algorithm concerning its denoising performance, as illustrated in Figure 6. In high-noise scenarios (e.g., input SNR < 25 dB), TFMD acts as an effective denoising tool. The output SNR, SNR_{out} , is consistently higher than the input SNR in this range, with the most significant improvement observed at the lowest SNRs, demonstrating the method’s capability to suppress substantial background noise. However, a performance trade-off emerges in low-noise (high SNR) conditions. For most cases, when the input SNR exceeds approximately 25-30 dB, the SNR_{out} begins to plateau and subsequently falls below the input SNR. This phenomenon suggests that the inherent reconstruction error of the TFMD process creates an error floor. When the noise level in the input signal is lower than this error floor, the artifacts introduced by the algorithm become more dominant than the original noise, leading to a net degradation in SNR_{out} .

Table 3: Performance metrics of TFMD for Case 4 under varying input SNR levels. Columns show the number of ground-truth modes (N_g), identified modes (N_f), total reconstruction error ($\mathcal{E}_{\text{rel, total}}$), and average mode error ($\mathcal{E}_{\text{rel, avg}}$).

Input SNR (dB)	N_g	N_f	$\mathcal{E}_{\text{rel, total}}$	$\mathcal{E}_{\text{rel, avg}}$
5	2	2	2.08×10^{-1}	2.04×10^{-1}
10	2	2	1.38×10^{-1}	1.39×10^{-1}
15	2	2	9.74×10^{-2}	9.61×10^{-2}
20	2	2	6.04×10^{-2}	6.14×10^{-2}
25	2	2	5.29×10^{-2}	5.29×10^{-2}
30	2	2	3.51×10^{-2}	3.59×10^{-2}
35	2	2	3.23×10^{-2}	3.30×10^{-2}
40	2	2	3.20×10^{-2}	3.25×10^{-2}

The numerical results in Table 3 provide a deeper insight into this behavior for the representative Case 4. A critical aspect of the algorithm’s robustness is its ability to consistently determine the correct number of constituent modes; the number of identified modes (N_f) precisely matches the number of ground-truth modes (N_g) across all tested noise levels. The table further shows that the reconstruction error decreases monotonically as the input SNR increases, with both the total reconstruction error, $\mathcal{E}_{\text{rel, total}}$, and the average mode error, $\mathcal{E}_{\text{rel, avg}}$. This continuous decrease in error, even when the SNR gain is no longer positive, confirms that the reconstructed signal becomes progressively closer to the noise-free ground truth as the input quality improves.

In summary, Experiment 2 reveals that the TFMD algorithm’s effectiveness is highly dependent on the noise level. It serves as a robust denoising tool in high-noise environments by improving the SNR. However, its performance is limited by an intrinsic error floor, which can reduce the SNR for input signals that are already very clean. Besides, the algorithm’s ability to consistently and accurately determine the number of constituent modes highlights its fundamental robustness in analyzing the structural composition of a signal.

4.3. Comparative Analysis with benchmark Algorithms

Experiment 3 provides a comprehensive comparative assessment of TFMD against several benchmark algorithms. The performance is evaluated based on the overall signal reconstruction quality, measured by the output SNR (SNR_{out}) and shown in Figure 7, and the fidelity of individual mode decomposition, measured by the average mode error ($\mathcal{E}_{\text{rel, avg}}$) and presented in Figure 8.

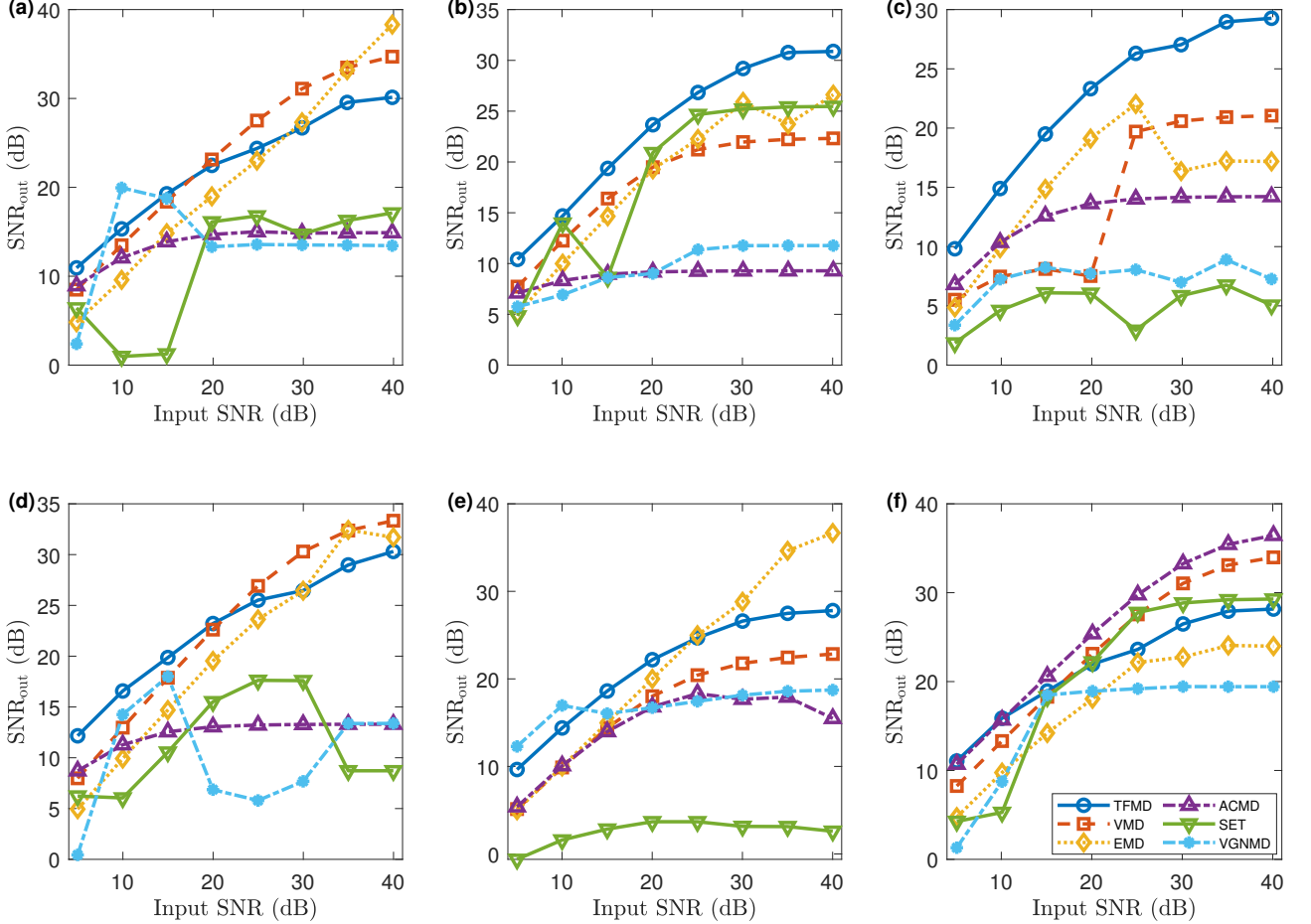


Figure 7: Comparative performance analysis from Experiment 3. SNR_{out} (dB) achieved by TFMD, VMD, EMD, ACMD, SET, and VGNMD as a function of input SNR (dB). Each subplot corresponds to one of the six synthetic signal cases described in Section 3.1.1: (a) Case 1, (b) Case 2, (c) Case 3, (d) Case 4, (e) Case 5, (f) Case 6. The legend identifying the methods is shown in subplot (f).

The analysis of the overall output SNR in Figure 7 reveals key performance characteristics. TFMD demonstrates strong performance, particularly in high-noise environments. In five out of the six test cases, TFMD achieves the highest SNR_{out} at the most challenging input SNR of 5 dB. The method also shows a distinct advantage when processing signals with complex modulations and transient features, as seen in Case 2 and Case 3, where TFMD generally outperforms the other methods across the SNR range.

To evaluate the fidelity of the reconstructed modes, the average mode error is examined in Figure 8, where a lower value indicates a more accurate decomposition. This analysis highlights the specialization of different algorithms. As expected, VGNMD demonstrates the best performance in Case 5, achieving the lowest average mode error, which aligns with its design

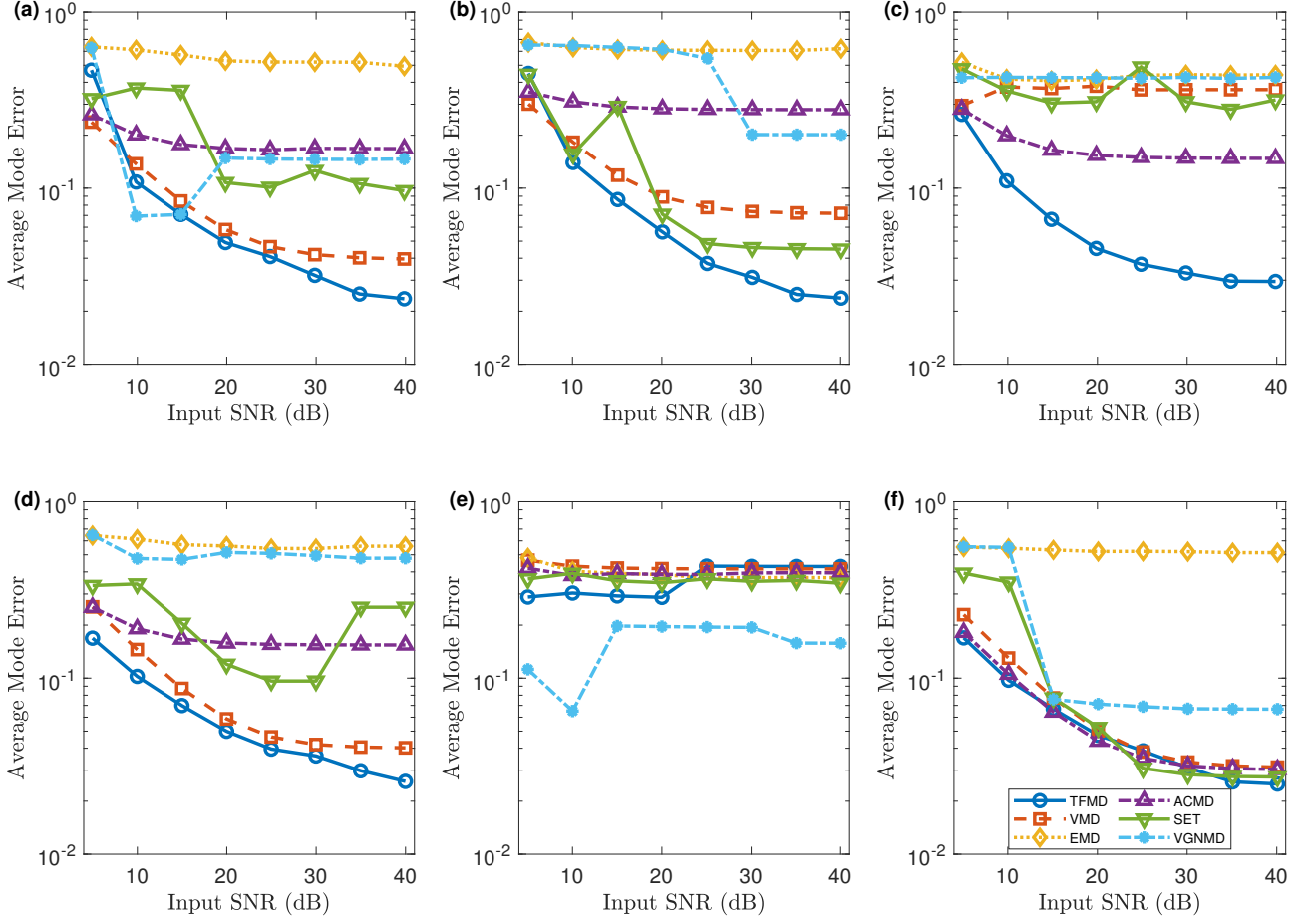


Figure 8: Comparative analysis of average mode error from Experiment 3. The plot shows the average relative L2 error, $\mathcal{E}_{\text{rel, avg}}$, for the reconstructed modes from each method as a function of input SNR. Lower values indicate higher fidelity in individual mode decomposition. Each subplot corresponds to one of the six synthetic signal cases, and the legend in subplot (f) identifies the methods.

for handling highly nonlinear signals. In contrast, TFMD showcases its strength in versatility and general robustness, consistently delivering low decomposition error across other cases (1, 2, 3, 4, and 6). This demonstrates that TFMD provides a reliable baseline performance across diverse signal types. The high errors exhibited by EMD and SET across all cases point to significant issues with mode mixing.

4.4. Application to Footbridge Vibration Signal

To demonstrate its practical utility, the prior-informed TFMD was applied to the target footbridge vibration signal. The method adaptively decomposed the signal into four distinct modes, as illustrated in Figure 9. An examination of the frequency spectrum for each reconstructed mode reveals that each is dominated by a single, sharp spectral peak. The frequencies of these peaks closely align with the first four natural frequencies of the Dowling Hall Footbridge previously identified in the literature [30]. Therefore, these four reconstructed modes can be reasonably considered to be the four dominant modal responses of the structure.

Figure 10 provides a direct comparison between the original processed signal and the signal reconstructed by summing these four modal responses. A key observation can be made from the magnitude spectra in Figure 10(b). While the primary spectral peaks corresponding to the modal responses are preserved in the reconstructed signal, the broadband noise floor between these peaks is significantly attenuated. This indicates that the TFMD process effectively acts as a denoising filter, isolating the coherent energy of the modal responses while discarding the diffuse, low-energy noise present in the original signal. This capability to extract cleaner modal responses from complex real-world data underscores the practical value of the proposed method for applications such as SHM.

5. Computational Complexity Analysis

To provide a rigorous basis for evaluating the computational efficiency of TFMD, this section presents a theoretical analysis of its time complexity, alongside that of the benchmark algorithms. The computational complexity of the proposed TFMD method is primarily determined by three sequential stages: the STFT, the CCL, and the ISTFT. For a signal of length T , an efficiently implemented STFT has a complexity of $O(T \log L_w)$. The CCL algorithm operates on the spectrogram—a grid with a total number of points proportional to T —and thus has a linear time complexity of $O(T)$. Finally, reconstructing K modes requires K separate ISTFT operations, each with a complexity of $O(T \log L_w)$. As TFMD is non-iterative, its total complexity is the sum of these parts, dominated by the K reconstruction steps.

In contrast, iterative methods such as EMD and ACMD have complexities that are directly proportional to the number of iterations, I , and the signal length, T . Their greedy, sequential extraction of K modes results in a total complexity of $O(K \cdot I \cdot T)$. VMD’s complexity is driven by the FFT/IFFT operations performed on the full signal at each iteration, leading to a complexity of $O(K \cdot I \cdot T \log T)$. More complex frameworks like SET and VGNMD, which rely

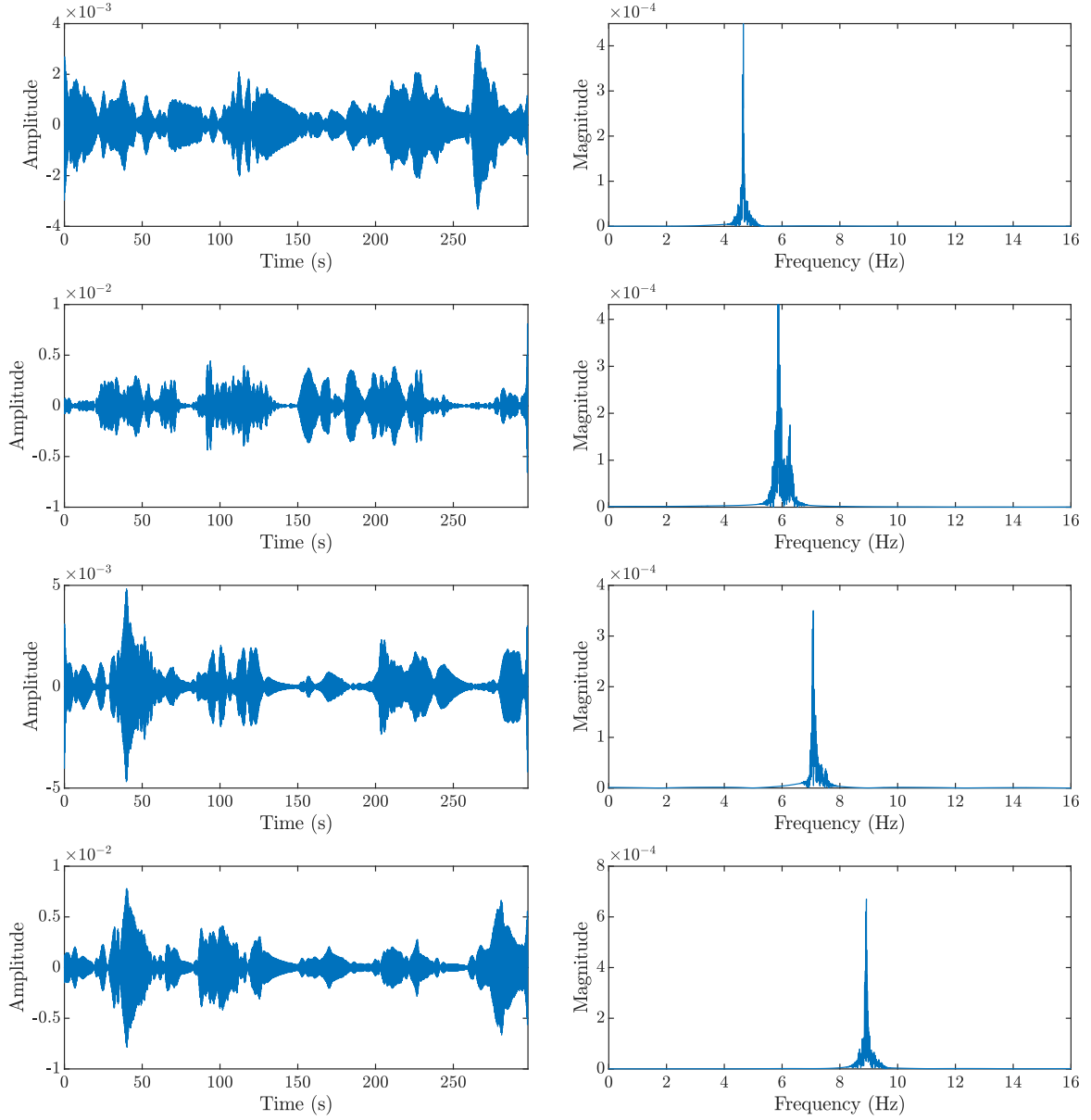


Figure 9: Modal responses extracted from the Dowling Hall Footbridge ambient vibration signal using prior-informed TFMD. Each row displays a reconstructed mode in the time domain (left) and its corresponding magnitude spectrum (right).

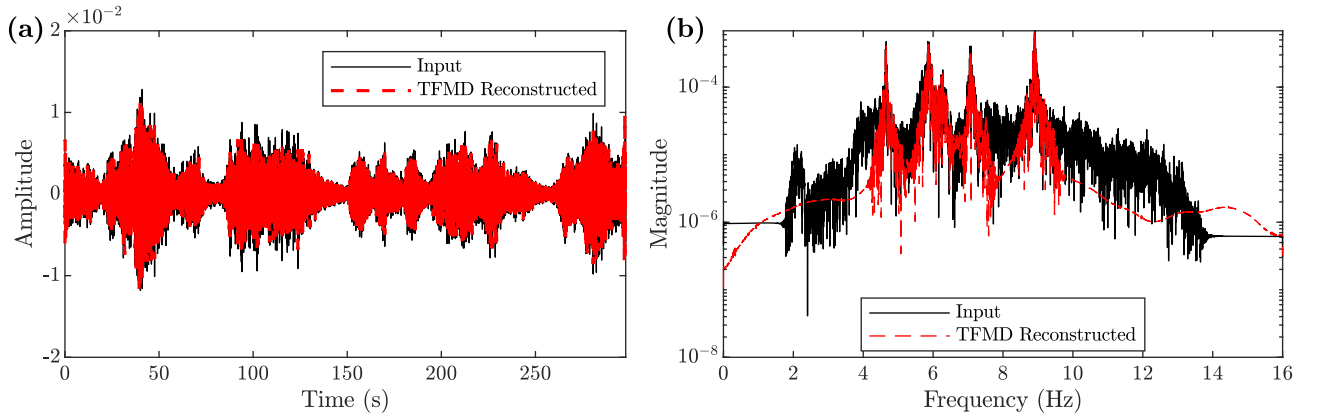


Figure 10: Comparison of the original processed signal and the TFMD reconstructed signal for the footbridge data. (a) Time-domain representation. (b) The corresponding magnitude spectra, plotted on a semi-logarithmic Y-axis to highlight the noise floor reduction.

on constructing a high-resolution time-frequency representation, exhibit a quadratic complexity ($O(T^2)$) due to the expensive computations required to analyze every time-frequency point.

A summary of the theoretical time complexities for TFMD and the benchmark algorithms is provided in Table 4. The analysis reveals that TFMD’s non-iterative, STFT-based pipeline results in a highly efficient, quasi-linear time complexity. This theoretical efficiency distinguishes TFMD from both the computationally intensive quadratic-complexity methods and the iterative methods, whose performance is contingent on their convergence rate.

Table 4: Theoretical time complexity of TFMD and benchmark signal decomposition algorithms.

Algorithm	Methodological Core	Time Complexity
TFMD	Non-iterative STFT masking via CCL	$O(K \cdot T \log L_w)$
ACMD	Greedy iterative variational method	$O(K \cdot I \cdot T)$
EMD	Greedy iterative sifting	$O(K \cdot I \cdot T)$
VMD	Parallel iterative variational method	$O(K \cdot I \cdot T \log T)$
SET	STFT post-processing	$O(T^2)$
VGNMD	Multi-stage hybrid	$O(T^2)$

* Notation: T is the signal length; K is the number of modes; I is the number of iterations; L_w is the STFT window length.

6. Discussion

The experimental results provide a comprehensive validation of the proposed TFMD methodology, highlighting its performance, underlying mechanisms, and comparative standing. This section discusses the interpretation and implications of these findings.

Decomposition Fidelity and Adaptivity. The results from noise-free signals establish TFMD’s high fidelity. The method accurately determined the number of constituent modes in all cases and reconstructed both the individual modes and the composite signal with low relative L2 errors. This success stems from its core strategy: isolating coherent, high-energy regions in the TF domain using a non-iterative pipeline of spectrogram smoothing, adaptive thresholding, and CCL. A key advantage of this approach is its data-driven adaptivity. The number of modes is not a required input but is discovered through the size-based filtering of candidate masks, which distinguishes TFMD from methods like VMD that require this a priori.

Noise Robustness and Performance Trade-offs. The analysis of noisy signals revealed a dual-faceted behavior. In high-noise environments, TFMD acts as an effective denoising tool, significantly improving the output SNR. This robustness is attributed to the spectrogram smoothing and mask filtering steps, which effectively separate structured, high-energy TF regions from diffuse or fragmented noise. However, the results also identified an error floor inherent to the method. At very high input SNRs, the small artifacts introduced by the STFT and binary masking process become more significant than the background noise, potentially leading to a decrease in the output SNR. Critically, even in these low-noise conditions, TFMD’s

ability to determine the correct number of modes remains unimpaired, demonstrating that its structural analysis capability is robust across all noise levels.

Comparative Performance and Practical Advantages. The comparative analysis positioned TFMD as a versatile and highly efficient algorithm. While specialized methods like VGNMD and ACMD showed superior reconstruction accuracy in their specific target scenarios, TFMD provided strong, often superior, performance across a broader range of signal types, particularly those with complex modulations and transients (Cases 2 and 3). Furthermore, the analysis of average mode error confirmed that TFMD excels at preserving the integrity of individual modes, a task where methods prone to mode mixing, such as EMD, consistently fail.

Perhaps the most significant practical advantage of TFMD is its computational efficiency, as established in the theoretical analysis in Section 5. Its non-iterative design and quasi-linear complexity of $O(K \cdot T \log L_w)$ make it exceptionally well-suited for real-time processing, the analysis of large datasets, or deployment on resource-constrained hardware. This combination of general robustness, high fidelity in mode separation, and superior theoretical efficiency establishes TFMD as a method offering a compelling and practical balance for real-world applications.

Application to Structural Health Monitoring. The application of TFMD to the footbridge vibration signal showcased its practical utility. The method successfully decomposed the signal into four distinct modes whose spectral characteristics closely matched the known natural frequencies of the structure, allowing them to be identified as the dominant modal responses. Importantly, the process also demonstrated a denoising effect, where the broadband noise floor in the original signal’s spectrum was attenuated in the reconstructed signal. This highlights TFMD’s potential as a valuable tool in SHM for extracting cleaner modal features from noisy ambient vibration signals.

Limitations and Future Work. Despite its strengths, TFMD has limitations that suggest avenues for future research. As an STFT-based method, its performance is dependent on the choice of windowing parameters, and boundary effects can influence reconstruction. The binary masking approach, while effective, does not denoise the content within the masked regions and could be challenged by severely overlapping (but not crossing) modes, which may be merged into a single mask. Future work could focus on developing automated, data-driven methods for selecting the few tuning parameters, exploring more advanced TF representations to improve resolution, and implementing more sophisticated segmentation logic to better handle closely spaced or overlapping components.

7. Conclusion

This paper introduced TFMD, a novel and computationally efficient framework for the adaptive decomposition of multicomponent signals. By reframing the problem as a time-frequency image segmentation task, the method employs a non-iterative pipeline of STFT, spectrogram smoothing, and mask generation via CCL and size-based filtering to automatically isolate and reconstruct the constituent modes.

Comprehensive validation using a suite of diverse synthetic signals and a real-world structural vibration signal demonstrated the method’s key capabilities. The main findings are:

1. **Adaptivity and Accuracy:** TFMD consistently and accurately determined the correct number of constituent modes across all test cases without requiring this information as a priori input. The reconstructed modes exhibited high fidelity, particularly in noise-free and high-noise scenarios.
2. **Robustness and Its Trade-offs:** The method serves as an effective denoising tool in high-noise environments. Its performance is, however, limited by an intrinsic error floor, which can affect the output SNR for signals that are already very clean.
3. **Versatility and Comparative Strength:** While specialized algorithms like ACMD and VGNMD excel in specific niches, TFMD demonstrated strong, often superior, performance across a broader range of signals, especially those containing complex modulations and transient components.
4. **Superior Computational Efficiency:** As a non-iterative method with a quasi-linear time complexity, TFMD is theoretically more efficient than benchmarked iterative and quadratic-complexity algorithms, making it highly suitable for large-scale and time-sensitive applications.
5. **Practical Utility:** The successful extraction of clean modal responses from a real-world footbridge vibration signal confirmed its applicability and value in practical engineering fields like SHM.

The primary strengths of TFMD lie in its compelling balance of adaptivity, general robustness, and exceptional computational efficiency. Future research could focus on automating the selection of its few parameters, integrating more advanced TF representations, and developing more sophisticated logic for separating severely overlapping modes. Nevertheless, this study establishes TFMD as a powerful and practical methodology for the analysis of complex multicomponent signals.

Acknowledgments

The authors are grateful for the financial support from Shenzhen Science and Technology Innovation Program through Grant No. JCYJ20220818100202006 and National Natural Science Foundation of China through Grant No. 12402483.

Conflicts of Interest

The authors declare no conflict of interest.

References

- [1] W. Zhou, Y. Xu, Damage identification for beam-like structures based on proper orthogonal modes of guided wavefields, *Mechanical Systems and Signal Processing* 189 (2023) 110052.

- [2] K. K. Patro, A. J. Prakash, G. Tummalapalli, P. L. Kumari, M. J. M. Rao, Detection of cardiac abnormalities in ecg signal using time-based signal processing algorithm, *International Journal of Computational Vision and Robotics* 15 (1) (2025) 59–74.
- [3] A. Ali, W. Xinhua, I. Razzaq, Optimizing acoustic signal processing for localization of precise pipeline leakage using acoustic signal decomposition and wavelet analysis, *Digital Signal Processing* 157 (2025) 104890.
- [4] F. Genovese, A. Palmeri, Wavelet-based generation of fully non-stationary random processes with application to seismic ground motions, *Mechanical Systems and Signal Processing* 223 (2025) 111833.
- [5] I. Amiri, A. N. Z. Rashed, Signal processing criteria based on electro-optic filters for fiber optic access transceiver systems, *Journal of Optical Communications* 45 (s1) (2025) s77–s83.
- [6] W. Zhou, Z. Feng, D. Liu, X. Wang, B. Chen, Modal parameter identification of structures based on short-time narrow-banded mode decomposition, *Advances in Structural Engineering* 23 (14) (2020) 3062–3074.
- [7] X.-Q. Shang, L. Tang, T.-L. Huang, N.-B. Wang, W.-X. Ren, Time-varying characteristics analysis of bridge under moving vehicle using a modified time-frequency method with limited sensors, *Engineering Structures* 316 (2024) 118528.
- [8] C. Wang, X. Pan, T.-Y. Qi, G.-N. Han, W.-X. Ren, Damage identification of simple supported bridges under moving loads based on variational mode decomposition and deep learning, *International Journal of Structural Stability and Dynamics* 25 (06) (2025) 2550065.
- [9] S. Chauhan, G. Vashishtha, R. Kumar, R. Zimroz, M. K. Gupta, P. Kundu, An adaptive feature mode decomposition based on a novel health indicator for bearing fault diagnosis, *Measurement* 226 (2024) 114191.
- [10] H. Wu, J. Cheng, N. Hu, Z. Cheng, Y. Yang, Quaternion empirical ramanujan fourier decomposition and its application in gear fault diagnosis, *Structural Health Monitoring* 23 (5) (2024) 2713–2736.
- [11] N. E. Huang, Z. Shen, S. R. Long, M. C. Wu, H. H. Shih, Q. Zheng, N.-C. Yen, C. C. Tung, H. H. Liu, The empirical mode decomposition and the hilbert spectrum for nonlinear and non-stationary time series analysis, *Proceedings of the Royal Society of London. Series A: Mathematical, Physical and Engineering Sciences* 454 (1971) (1998) 903–995.
- [12] Z. Wu, N. E. Huang, Ensemble empirical mode decomposition: a noise-assisted data analysis method, *Advances in Adaptive Data Analysis* 1 (01) (2009) 1–41.

- [13] M. E. Torres, M. A. Colominas, G. Schlotthauer, P. Flandrin, A complete ensemble empirical mode decomposition with adaptive noise, in: 2011 IEEE International Conference on Acoustics, Speech and Signal Processing (ICASSP), IEEE, 2011, pp. 4144–4147.
- [14] K. Dragomiretskiy, D. Zosso, Variational mode decomposition, *IEEE Transactions on Signal Processing* 62 (3) (2013) 531–544.
- [15] S. Chen, X. Dong, Z. Peng, W. Zhang, G. Meng, Nonlinear chirp mode decomposition: A variational method, *IEEE Transactions on Signal Processing* 65 (22) (2017) 6024–6037.
- [16] J. Gilles, Empirical wavelet transform, *IEEE Transactions on Signal Processing* 61 (16) (2013) 3999–4010.
- [17] W. Zhou, Z. Feng, Y. Xu, X. Wang, H. Lv, Empirical fourier decomposition: An accurate signal decomposition method for nonlinear and non-stationary time series analysis, *Mechanical Systems and Signal Processing* 163 (2022) 108155.
- [18] P. Singh, S. D. Joshi, R. K. Patney, K. Saha, The fourier decomposition method for nonlinear and non-stationary time series analysis, *Proceedings of the Royal Society A: Mathematical, Physical and Engineering Sciences* 473 (2199) (2017) 20160871.
- [19] J. Cheng, Y. Yang, Z. Wu, H. Shao, H. Pan, J. Cheng, Ramanujan fourier mode decomposition and its application in gear fault diagnosis, *IEEE Transactions on Industrial Informatics* 18 (9) (2021) 6079–6088.
- [20] I. Daubechies, J. Lu, H.-T. Wu, Synchrosqueezed wavelet transforms: An empirical mode decomposition-like tool, *Applied and Computational Harmonic Analysis* 30 (2) (2011) 243–261.
- [21] G. Yu, Z. Wang, P. Zhao, Multisynchrosqueezing transform, *IEEE Transactions on Industrial Electronics* 66 (7) (2018) 5441–5455.
- [22] G. Yu, M. Yu, C. Xu, Synchroextracting transform, *IEEE Transactions on Industrial Electronics* 64 (10) (2017) 8042–8054.
- [23] G. Yu, T. R. Lin, Second-order transient-extracting transform for the analysis of impulsive-like signals, *Mechanical Systems and Signal Processing* 147 (2021) 107069.
- [24] Y. Ma, G. Yu, T. Lin, Q. Jiang, Synchro-transient-extracting transform for the analysis of signals with both harmonic and impulsive components, *IEEE Transactions on Industrial Electronics* 71 (10) (2024) 13020–13030.
- [25] H. Wang, S. Chen, W. Zhai, Variational generalized nonlinear mode decomposition: Algorithm and applications, *Mechanical Systems and Signal Processing* 206 (2024) 110913.

- [26] H. Wang, S. Chen, W. Zhai, Improved variational generalized nonlinear mode decomposition for separating crossed chirp modes and dispersive modes of non-stationary signals in mechanical systems, *Mechanical Systems and Signal Processing* 227 (2025) 112407.
- [27] C. Xu, Y. Liao, Nonlinear chirp mode extraction: A new efficient method to decompose nonstationary signals, *Signal Processing* (2025) 109943.
- [28] J. B. Allen, L. R. Rabiner, A unified approach to short-time fourier analysis and synthesis, *Proceedings of the IEEE* 65 (11) (1977) 1558–1564.
- [29] R. M. Haralick, L. G. Shapiro, Connected components labeling, *Computer and Robot Vision* 1 (1992) 28–48.
- [30] P. Moser, B. Moaveni, Environmental effects on the identified natural frequencies of the dowlings hall footbridge, *Mechanical Systems and Signal Processing* 25 (7) (2011) 2336–2357.
- [31] B. Moaveni, I. Behmanesh, Effects of changing ambient temperature on finite element model updating of the dowlings hall footbridge, *Engineering Structures* 43 (2012) 58–68.
- [32] S. Chen, Y. Yang, Z. Peng, S. Wang, W. Zhang, X. Chen, Detection of rub-impact fault for rotor-stator systems: A novel method based on adaptive chirp mode decomposition, *Journal of Sound and Vibration* 440 (2019) 83–99.